Spray formation in a quasiplanar gas-liquid mixing layer at moderate density ratios: A numerical closeup

Yue Ling,* Daniel Fuster, and Stéphane Zaleski†
Sorbonne Universités, UPMC Université Paris 06, CNRS, UMR 7190, Institut Jean Le Rond d'Alembert, F-75005 Paris, France

Grétar Tryggvason
Department of Aerospace and Mechanical Engineering, University of Notre Dame, Notre Dame, Indiana 46556, USA
(Received 18 July 2016; published 23 January 2017)

The three-dimensional development of instabilities and the subsequent spray formation in a gas-liquid mixing layer are important fundamental problems in the area of multiphase flows. It is highly desirable to visualize this detailed atomization process and to analyze the instabilities and mechanisms involved, and massive numerical simulations are required, in addition to experiment. Rapid development of numerical methods and computer technology in the past decade now allows large-scale three-dimensional direct numerical simulations of atomization to be performed. Nevertheless, the fundamental question, whether all the physical scales involved in the primary breakup process are faithfully resolved, has eluded researchers until now. In the present study, we conduct direct numerical simulations of spray formation in a gas-liquid mixing layer with state-of-the-art computational resources (using up to 4×10^9 cells and 16 384 cores), in order to obtain a high-fidelity numerical closeup of the detailed mechanisms of spray formation. We also aim to examine whether present computational resources are sufficient for a fully resolved direct numerical simulation of atomization.

DOI: 10.1103/PhysRevFluids.2.014005

I. INTRODUCTION

The breakup of fluid masses is a phenomenon of enormous complexity, with diverse physical setups and mechanisms. When the fluid masses break rapidly into large numbers of small droplets one speaks of atomization [1,2]. Such atomization in a gas-liquid mixing layer, where a high-speed gas stream emerges from an orifice parallel to a lower-speed liquid stream, has been studied in great detail [3,4]. The resulting Kelvin-Helmholtz instability generates large coherent structures that grow in size as they propagate downstream, together with equally growing wavelike structures [5] on the liquid-gas interface. The standard picture of atomization [1] is that two-dimensional wave structures form near the orifice, develop into sheets, which in turn develop Taylor-Culick end rims. The flow then becomes more markedly three dimensional: finger branching from the end rim and then various threads, fibers, or ligamentlike structures parallel to the flow appear, which eventually break into droplets. This sequence and its variants are called primary atomization, which is supposed to be followed by secondary atomization, the breakup of large drops further downstream whenever they interact with sufficiently high-velocity gas flow. Several types of probability distributions of droplet sizes have been proposed and compared to experiments [3,6]. Another mechanism for primary atomization is the formation of holes in the thin-sheet-like structures that appear in the waves prior

*Present address: Department of Mechanical Engineering, Baylor University, Waco, Texas 76798, USA; stanley_ling@baylor.edu
†stephane.zaleski@upmc.fr

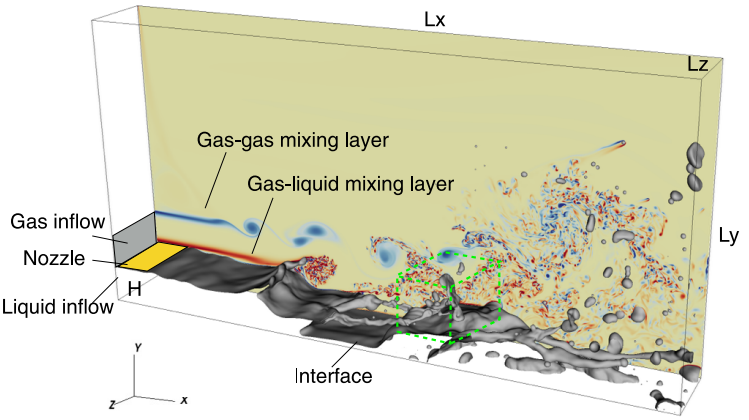

FIG. 1. Spray formation in a gas-liquid mixing layer. The z vorticity is shown on the backplane. The sampling region for droplets statistics is indicated by green dashed lines.

to the formation of ligaments and fingers. These holes in thin-sheet structures are quite similar, but not identical, to the holes that form in bag-breakup secondary atomization [7] and in splashes [8]. The hole formation has not been visualized as frequently in primary atomization and is thus less firmly documented.

In order to better understand the mechanisms underlying atomization, experimentalists have switched from the coaxial round jets typical of industrial applications to a quasiplanar setup that is more favorable for detailed analysis [9–11]. This setup has allowed precise measurements and detailed visualizations of the droplet-forming process. In the quasiplanar configuration it is possible to compare the growth and frequency of the Kelvin-Helmholtz instability in the linear regime as predicted by numerical simulation, linear stability theory, and experiments [12]. Three-dimensional analysis is, for obvious reasons [13–15], less advanced, despite a large number of results in the references already cited. In this work we simulate a model of the quasiplanar experiment of Matas *et al.* [9] in order to better understand the mechanisms of droplet formation.

II. METHODOLOGY

A. Problem description and simulation setup

The computational setup of the present problem is shown in Fig. 1. The domain is a box of dimensions $L_x \times L_y \times L_z$, where we inject two streams, liquid and gas, separated by a solid separator plate of size $\ell_x \times \ell_y \times L_z$. The liquid and gas streams enter through the boundary at $x = 0$. The thickness of the liquid stream is H, while that for the gas stream is $H - \ell_y$.

The inflow velocity is specified as $(u_{\text{inflow}},0,0)$ at the left boundary of the domain, where the streamwise component $u|_{\text{inflow}}$ is expressed as

$$u_{\text{inflow}} = \begin{cases} U_l \operatorname{erf}\frac{2(H-y)}{\delta}, & 0 \leqslant y < H \\ U_g \operatorname{erf}\frac{2(y-H-l_y)}{\delta} \operatorname{erf}\frac{2(2H-y)}{\delta}, & H \leqslant y < 2H \\ 0, & y > 2H. \end{cases} \tag{1}$$

The outflow condition is invoked at the right ($x = L_x$). The bottom boundary ($y = 0$) is taken as a slip wall and periodic boundary conditions are applied to the front and the back ($z = 0$ and L_z). In order to minimize the effect of the finite size of the domain, the dimensions of the box are large in the x and y dimensions $L_x = 16H$ and $L_y = 8H$, respectively (while L_z is set to $2H$). Furthermore, we

TABLE I. Physical parameters.

ρ_l (kg/m^3)	ρ_g (kg/m^3)	μ_l (Pa s)	μ_g (Pa s)	σ (N/m)	$U_{0,l}$ (m/s)	$U_{0,g}$ (m/s)	H (m)	δ_g (m)	l_y (m)
1000	50	10^{-3}	5×10^{-5}	0.05	10	0.5	8×10^{-4}	2×10^{-4}	2.5×10^{-5}

allow the fluid to freely enter or leave the top boundary ($y = L_y$) by applying a Neumann boundary condition for the normal velocity.

The boundary layers of the injected streams are represented by an error function. The thickness of the boundary layers on the liquid and gas sides of the separator plate are taken to be identical and denoted by δ and we set $\delta = H/4$. The length ℓ_x and the thickness ℓ_y of the separator plate are $H/2$ and $H/32$, respectively, and it has been shown that the details of the separator plate are immaterial to the atomization process as long as $\ell_y \ll \delta$ [12].

It is infeasible with the present computational capability and numerical methodology to perform direct numerical simulations (DNSs) in this setup using the physical parameters exactly as in the experiments [9]. This is due to the very wide range of relevant physical scales. Indeed, the tiny submicron droplets generated are four orders of magnitudes smaller than H. A three-dimensional (3D) mesh to resolve such a wide range of length scales would easily exceed 10^9 cells (for $H = 1$ cm and the cell size $\Delta \approx 1\ \mu$m); the computational cost for such simulations is clearly far beyond the current computer power. To alleviate these problems we reduce the physical scale ($H = 0.8$ mm is used here compared to $H = 5$–20 mm in experiments [9]) and choose a set of parameters that allows faster and easier simulations while still placing the flow in the high-speed atomization regime. (As shown later, even for the reduced-scale setup here we barely achieved well-resolved results using 16 384 cores.) The physical parameters and the corresponding dimensionless parameters are given in Tables I and II, using standard notation and international units.

B. Numerical methods

We solve the Navier-Stokes equations for incompressible flow with sharp interfaces and constant surface tension using the volume-of-fluid method as described in Tryggvason *et al.* [16]. The fields are discretized using a fixed regular cubic grid (with cell size Δ) and we use a projection method for the time stepping to incorporate the incompressibility condition. The temporal integration is conducted by a second-order predictor-corrector method [16]. The interface is tracked using a volume-of-fluid (VOF) method with a mixed Youngs-centered implementation of Aulisa *et al.* [17] to determine the normal vector and a Lagrangian-explicit scheme of Li [18] for the VOF advection [19]. The advection of momentum near the interface is conducted in a manner consistent with the VOF advection [20] with the superbee limiter applied in flux calculation. The viscous term is treated explicitly. Curvature is computed using the height-function method by Popinet [21]. Surface tension is computed from curvature by a balanced continuous-surface-force method (see the works of Renardy and Renardy [22], Francois *et al.* [23], and Popinet [21]). Density and viscosity are computed from the VOF fraction by an arithmetic mean. To capture the dynamics of poorly resolved droplets accurately, droplets of size smaller than four cells are converted to Lagrangian point particles [24]. The overall

TABLE II. Key dimensionless parameters.

M $\rho_g U_g^2/\rho_l U_l^2$	r ρ_l/ρ_g	m μ_l/μ_g	$\mathrm{Re}_{g,\delta}$ $\rho_g U_g \delta/\mu_g$	$\mathrm{We}_{g,\delta}$ $\rho_g U_g^2 \delta/\sigma$	Re_g $\rho_g U_g H/\mu_g$
20	20	20	2000	20	8000

TABLE III. Summary of simulation runs.

Run	Δ (μm)	H/Δ	No. of cells	No. of cores	Total core hours
M0	25	32	8.39×10^6	32	$\sim 6 \times 10^3$
M1	12.5	64	6.71×10^7	256	$\sim 1 \times 10^5$
M2	6.25	128	5.37×10^8	2048	$\sim 1.7 \times 10^6$
M4	3.125	256	4.29×10^9	16384	$\sim 14 \times 10^6$

method is implemented in the free code PARIS [25] and validation studies can be found in the work of Ling *et al.* [24].

C. Simulation cases and computational costs

To assess whether the present simulation is a full DNS of atomization, simulations are performed on four grids called M0, M1, M2, and M3 so that Mn has $H/\Delta = 32 \times 2^n$ points in the liquid layer H (see Table III). The time step for each mesh is computed based on the Courant-Friedrichs-Lewy (CFL) condition, i.e., $|\boldsymbol{u}|_{\max}\Delta t/\Delta < \theta$, where θ is the CFL number, which is taken to be 0.4 for all cases. The average time steps for the M0, M1, M2, and M3 meshes are approximately 0.53, 0.28, 0.14, and 0.068 μs, respectively.

The domain is initially filled with stationary gas (at $t = 0$) and then liquid and gas streams progressively enter it. It takes a period of about 16 ms for the flow to reach a statistically steady state (more details are shown in Sec. III A). For the M0, M1, and M2 meshes, the simulations all start from $t = 0$ and end at about $t = 70$ ms. For the M3 mesh, the simulation was performed using about 4×10^9 cells using 16 384 processors. Due to the extreme cost for the M3 simulation, the simulation starts from a checkpoint of the M2 simulation at about $t = 16$ ms and is continued only up to about $t = 28$ ms.

The M3 simulations are split into multiple runs, which are conducted on the supercomputers CINECA-FERMI in Italy, LRZ-superMUC in Germany, and TGCC-CURIE in France. The M0, M1, and M2 simulations are all performed on TGCC-CURIE. The total simulation time for all four meshes takes over 15×10^6 CPU hours. The results presented correspond to the M3 mesh, unless stated otherwise.

III. RESULTS

A. Overall atomization process

A global view of the atomization in a gas-liquid mixing layer is shown in Fig. 1. The single-phase (gas-gas) and the two-phase (gas-liquid) mixing layers can be identified from the z vorticity plotted on the backplane. Both of the mixing layers are unstable due to the velocity difference across the layers. The gas-liquid mixing layer develops faster and evolves a Kelvin-Helmholtz-like wave on the interface. The interfacial wave grows and a thin liquid sheet forms at the wave crest. A Taylor-Culick rim appears at the edge of the liquid sheet. The sheet folds and creases under the action of the turbulent gas stream, which leads to perturbations of the rim. These perturbations produce small fingers that later develop into long ligaments. There is an important difference between the rim instabilities observed here and those seen, for example, in droplet splashes where interaction with energetic air motion is absent. The ligaments eventually break into small droplets due to Rayleigh-Plateau instability. The unbroken part of the liquid sheet reattaches to the domain bottom. Compared to the gas-liquid mixing layer, the gas-gas mixing layer evolves more slowly. The invasion of the turbulent vortices from the gas-liquid mixing layer accelerates the development of the gas-gas mixing layer. Eventually, the two mixing layers merge and the downstream flows become fairly violent and chaotic.

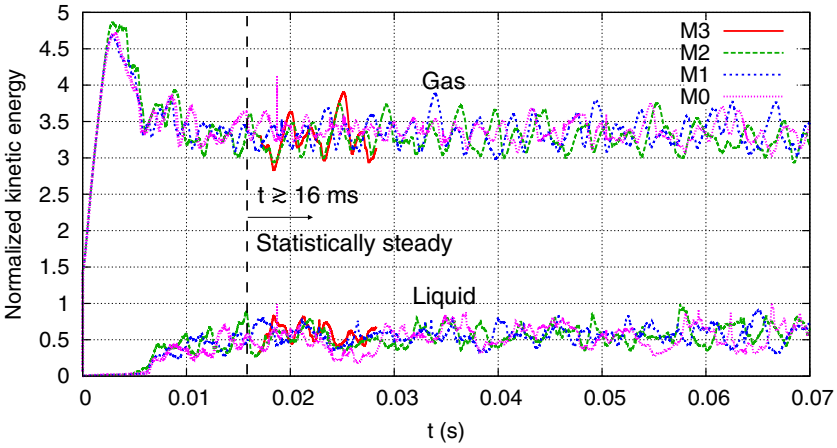

FIG. 2. Temporal evolution of the mean kinetic energy of gas and liquid over the computational domain for different meshes. The kinetic energy is normalized by U_g^2.

The domain is initially filled with stationary gas and the liquid and gas streams are then injected progressively. As a result, it takes a transition time for the turbulent multiphase flow and the resulting atomization processes to reach a statistically steady state. The temporal evolutions of the average gas and liquid kinetic energy over the whole domain, i.e., $\frac{1}{\mathbb{V}U_g^2}\int_{\mathbb{V}}\frac{u^2}{2}(1-C)dV$ and $\frac{1}{\mathbb{V}U_g^2}\int_{\mathbb{V}}\frac{u^2}{2}C\,dV$, are shown in Fig. 2, where C and $\mathbb{V}$ represent the liquid volume fraction and the volume of the computational domain, respectively. It is shown that both the gas and liquid kinetic energy reach an approximate steady state at about $t = 16$ ms. The simulations for the M0, M1, and M2 meshes are then continued to $t = 70$ ms. Due to the extreme cost of the M3 case, the simulation is run only up to about $t = 28$ ms.

The formation, development, and breakup of the sequential interfacial waves significantly perturb the gas flow, resulting in the large-scale low-frequency oscillations in the temporal evolution of the gas or liquid kinetic energy (the small-scale high-frequency oscillations may be due to turbulence and its interaction with the wave). Therefore, we can approximately estimate the number of waves captured by the simulation. For the M0, M1, and M2 meshes, about 20 waves are captured after the steady state is reached. For the M3 mesh, due to the shorter simulation time, only about four waves are observed.

B. Formation of sheets

Due to the velocity difference between the gas and liquid across the interface, a Kelvin-Helmholtz-like wave develops on the interface and propagates downstream. As the interfacial wave grows, the radius of curvature at the wave crest continues to decrease and eventually liquid sheets form.

It is generally believed that the wave that appears first is a two-dimensional one and then transverse instabilities (such as Rayleigh-Taylor and Rayleigh-Plateau instabilities) develop at the rim of the liquid sheet. This quasi-2D wave and its development are shown in Figs. 3(a)–3(d). The temporal evolution of the wave can be seen more clearly by a sequence of snapshots of the interface at the plane $z = H$ [see Fig. 3(e)]. The wave initially takes a Gaussian-like shape. The minimum radius of curvature is located near the wave crest and decreases from 189.7 μm at 17.3 ms to 43.1 μm at 17.6 ms. Then the wave tends to fold forward. At a time between 17.7 and 17.9 ms, the two interfaces on both sides of the wave crest become parallel and form a liquid sheet. At this point, the thickness of the liquid sheet, denoted by e, is 174 μm. As the sheet is pulled and stretched by the fast gas stream, its thickness decreases in time. At $t = 18.2$ ms [the last profile in Fig. 3(e)] the minimum sheet thickness decreases to about 50 μm. At this scale the capillary time is $\tau_{ca} = (\rho_l e^3/\sigma)^{1/2} \approx 0.05$ ms

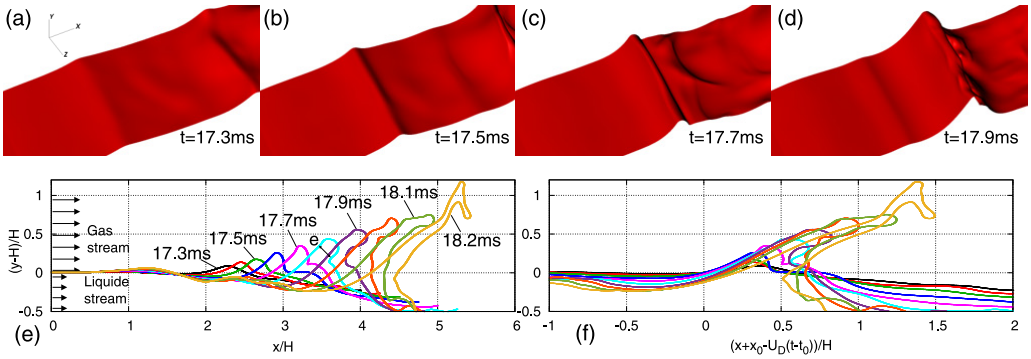

FIG. 3. Development of a quasi-2D interfacial wave, forming a liquid sheet: (a)–(d) time snapshots of the interface; interface profiles at plane $z = H$ with (e) the original scale and (f) the x axis scaled by the Dimotakis speed U_D.

and the Ohnesorge number is $\mathrm{Oh} = \mu_l(\sigma\rho_l e)^{-1/2} \approx 0.02$. There are still $e/\Delta = 16$ grid points for the sheet thickness. It can be seen that at this time of $t = 18.2$ ms the tip of the liquid sheet starts to fold. The radius of curvature at the hinge point is about 25 μm. The fact that the tip of the sheet folds, instead of forming a Taylor-Culick end rim as expected for this time scale and Oh number, is a testimony to the strong interaction of the liquid sheet with the gas stream. The wave amplitude at $t = 18.2$ ms is comparable to H bringing the interaction to a maximum.

The celerity of the interfacial wave is approximately a constant and agrees well with the Dimotakis speed

$$U_D = \frac{U_l + \sqrt{r}U_g}{1 + \sqrt{r}}, \tag{2}$$

which is about 2.23 m/s for the present case. If the x axis is shifted by U_D with respect to the origin of wave formation x_0 and t_0, the waves at different times collapse, except the amplitude, as shown in Fig. 3(f). The agreement between the computed interfacial wave celerity with the Dimotakis speed is a robust observation affirmed by other waves captured in the simulation. This is also consistent with the well-documented 2D case [10].

Beyond the conventionally known quasi-2D waves, it is observed from the simulation results that the liquid sheet also forms in a fully three-dimensional manner [see Figs. 4(a)–4(d)], resulting in a significant transversely deforming rim at the sheet edge. This transverse wavelength is of the order of the width of the domain. (This may indicate that the domain width is too small for the long-wavelength modes in transverse instabilities.) It has been shown before that the Rayleigh-Plateau instability can induce transverse deformation of the rim, which later develops into fingers [26,27]. However, here the formation of 3D structures is clearly much faster than the Rayleigh-Plateau rim instability would be and even occurs before the rim is formed at about $t = 19.6$ ms in Fig. 4(c).

Other different mechanisms can contribute to the formation of the 3D wave. In particular, it has been shown by the transient growth theory that the 3D perturbations of a two-phase mixing layer can be more unstable than the 2D ones [28].

Furthermore, the turbulent gas flow on top of the interface impose significant 3D forcing on the interfacial wave. As the Reynolds number of the gas boundary layer is large ($\mathrm{Re}_\delta = 2000$), the gas stream becomes turbulent at about $x/H = 2{-}3$. Two instantaneous turbulent vortical structures of the gas flow above the interface are shown in Figs. 4(e) and 4(f). Due to the low speed of the liquid stream, the interface serves as a deformed "wall" and imposes a shear to the gas flow like in typical turbulent boundary layers. As a result, the early streamwise development of vortices is quite similar to that observed in turbulent boundary layers [29]. Quasistreamwise vortices near the transition region [30] can be clearly seen in Fig. 4(e). The footprints of these turbulent vortices

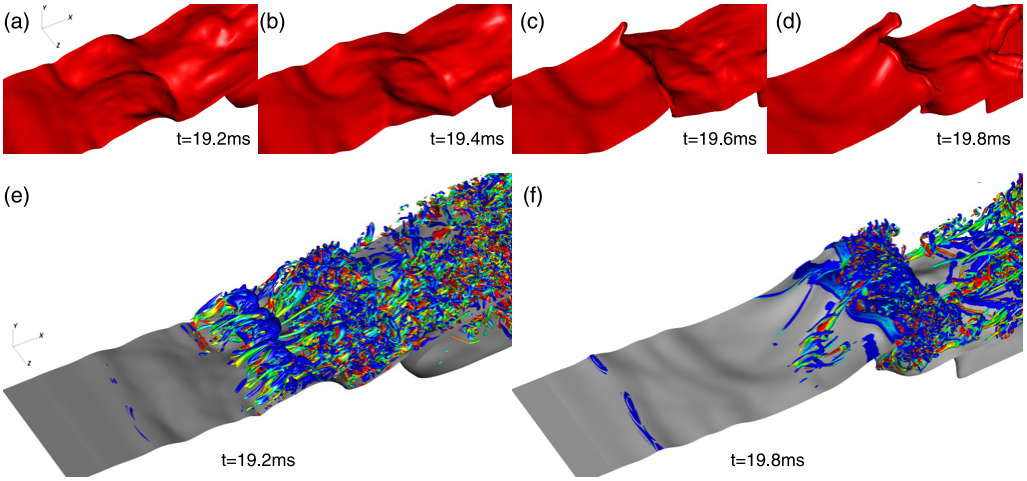

FIG. 4. Development of a fully 3D interfacial wave: (a)-(d) time snapshots of the interface and (e) and (f) turbulent vortical structures in the gas-liquid mixing layer (visualized by the λ_2 criterion).

on the interface can be clearly seen in Fig. 4(a), which corresponds to the same time snapshot as Fig. 4(e), evidencing the effect of the gas turbulence on perturbing the interface. The later growth of the interfacial wave introduces significant modulation to the gas turbulence, for example, the flow separation downstream of the wave enhances turbulence development [see Fig. 4(f)]. The interaction between turbulence and the interfacial wave formation is very complex and is beyond the scope of the present paper.

Finally, complex capillary wave interactions on the interface also contribute to triggering irregular 3D waves. As shown in Fig. 5, the capillary waves propagate both upstream (waves A and C) and downstream (wave B). The capillary wave speed can be estimated as

$$U_{\mathrm{ca}} = \sqrt{\frac{\pi\sigma}{\rho_l \lambda}}, \tag{3}$$

where λ is the wavelength. For $\lambda = 2\Delta_{\mathrm{M2}}$, $U_{\mathrm{ca}} \approx 3.54$ m/s. Therefore, small-scale capillary waves indeed can overcome the Dimotakis speed ($U_D \approx 2.23$ m/s) and move upstream. The upstream and downstream propagating waves B and C meet and accelerate the development of the C wave.

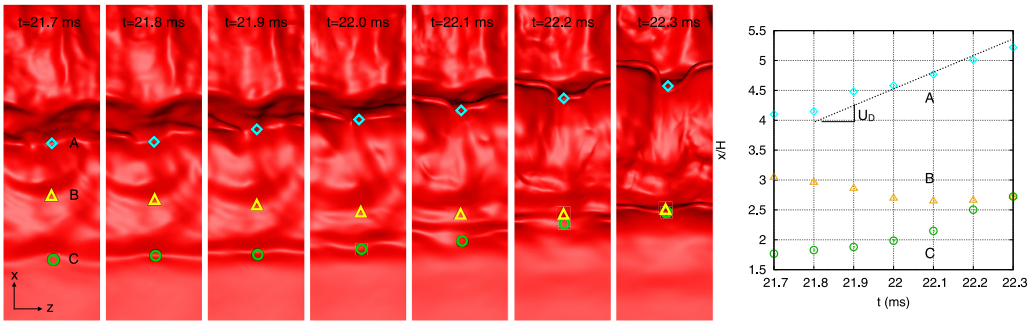

FIG. 5. Interfacial waves interaction (results by the M2 mesh). Symbols indicate locations of the wave crests at plane $z = H$. The Dimotakis speed (black dashed line) is plotted for comparison.

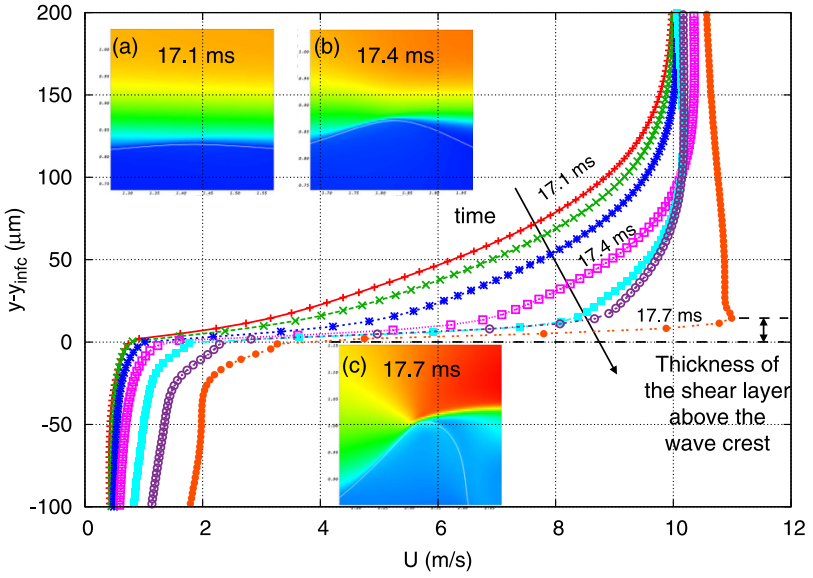

FIG. 6. Temporal evolution of the shear layer near the wave crest. (a)–(c) Streamwise velocity contours near the wave crest (gas-liquid interfaces are indicated by white lines). The line plots are the streamwise velocity profiles in the y direction at the wave crest. The y location of the interface is denoted by y_{infc}.

C. Effect of mesh resolution

It has been shown previously that the boundary layer of the injected gas stream must be well resolved, since otherwise the gas-assisted atomization and the frequency of the interfacial instability will not be accurately captured [12]. In the present study, we found that requiring sufficient numerical resolution to compute the formation of the sheet and the rim indeed introduces a stricter requirement on mesh size. As shown in Fig. 3(b), the radii of the wave crest can go down to about 43.1 μm ($t = 17.6$ ms) or even lower to 25 μm when the sheet folds, which is much smaller than the injected gas boundary layer thickness δ ($\approx 200\,\mu$m). Furthermore, the thickness of the shear layer above the wave crest significantly decreases as the wave develops (see Fig. 6). The shear layer thickness is initially similar to the boundary layer thickness of the injected gas stream δ (see $t = 17.1$ ms) and then it drops rapidly as the wave grows to about 15 μm at $t = 17.7$ ms. The M0 mesh ($\Delta = 25\,\mu$m) is clearly insufficient to resolve the wave crest curvature and the shear layer; as a result, the formation of the sheet is not properly captured. As shown in Fig. 7(a), the rim is completely missed and the tip of the liquid sheet breaks erroneously, forming numerous tiny ligaments and droplets. The result for the M1 mesh ($\Delta = 12.5\,\mu$m) is better, but two sides of the rim are still poorly resolved. For the M2 and M3 meshes ($\Delta = 6.25$ and $3.125\,\mu$m), about four and seven cells, respectively, are used to resolve the minimum radius of the wave and about three and six cells for the shear layer above the

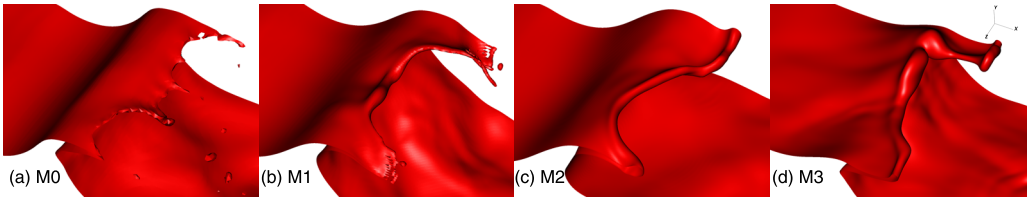

FIG. 7. Close-up at the sheet formed at the wave crest for different mesh resolution.

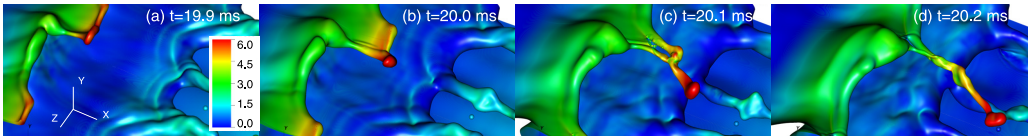

FIG. 8. Ligaments formation due to fingering at the tip of a liquid sheet. The color on the interface indicates the streamwise velocity.

wave crest. As a result, the sheet formation and the rim dynamics are well captured [see Figs. 7(c) and 7(d)]. In such cases, no fingers or droplets are formed at this early stage.

D. Formation of ligaments

The transverse instability of the rim is known to generate fingers at the tip of a liquid sheet [27]. The formation of a finger at the rim is well captured by the present simulation as shown in Fig. 8. The streamwise fluid velocity is also plotted on the interface and it can be seen that the velocity increases gradually from the base to the round tip of the finger, indicating that the finger is stretched by the surrounding fast gas stream. Eventually, the short finger develops into a long ligament, which breaks later to form droplets.

Beyond fingering at the rim of the liquid sheet, holes appearing in the liquid sheet are observed to be another way to break the liquid sheet and to produce ligaments. Similar to the fingers, the liquid sheet is also stretched by the gas stream and becomes thinner and thinner. At a certain stage, holes are formed in the liquid sheet (see Fig. 9). The two holes are initially very small (highlighted by different dashed lines) but later they expand rapidly, causing the liquid sheet to rupture. Several small ligaments are generated and the orientations of these ligaments are more diverse, different from the ligaments formed by fingering, which tend to align with the streamwise direction.

For a stationary liquid sheet, holes are formed only when the sheet thickness is very small [$e \sim O(10)$ nm] and the disjoining pressure becomes active. For a dynamic liquid sheet it has been shown in recent experiments that holes can form at a much larger thickness [$e \sim O(10)\,\mu$m] [7,8]. For example, in the experiment on splashes by Marston *et al.* [8], the sheet thickness estimated by the hole expansion velocity and the Taylor-Culick theory is about $9-16\,\mu$m. Several effects may explain the piercing of a liquid sheet at such large thicknesses, including Marangoni effects and perturbations from bubbles or droplets too small to be visible. Random perturbations from unseen objects are difficult to model and Marangoni forces are not included in the present simulation. Here holes appear when the thickness of the liquid sheet decreases to about the cell size Δ. This numerical cutoff length scale (the smallest Δ used is about 3.1 μm) is much larger than breakup thickness of a stationary sheet but is comparable to or even smaller than the length at which dynamic liquid sheets are seen to break in experiments.

An example of the evolution of a hole formed in a liquid sheet is shown in Fig. 10. The measured hole expansion velocities in the streamwise and transverse directions are $U_{h,x} \approx 2.70$ m/s and $U_{h,z} \approx 0.978$ m/s, respectively. As can be seen from the cross sections of the hole in the y-z and x-y planes, the sheet thickness near the hole is very uneven. The minimum sheet thickness just before

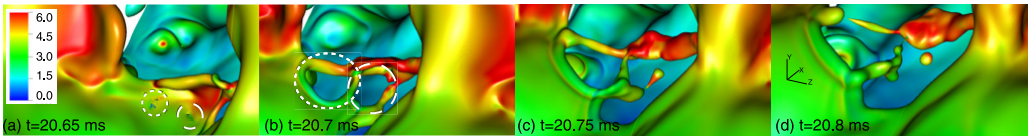

FIG. 9. Ligaments formation due to holes in a liquid sheet. The color on the interface indicates the streamwise velocity.

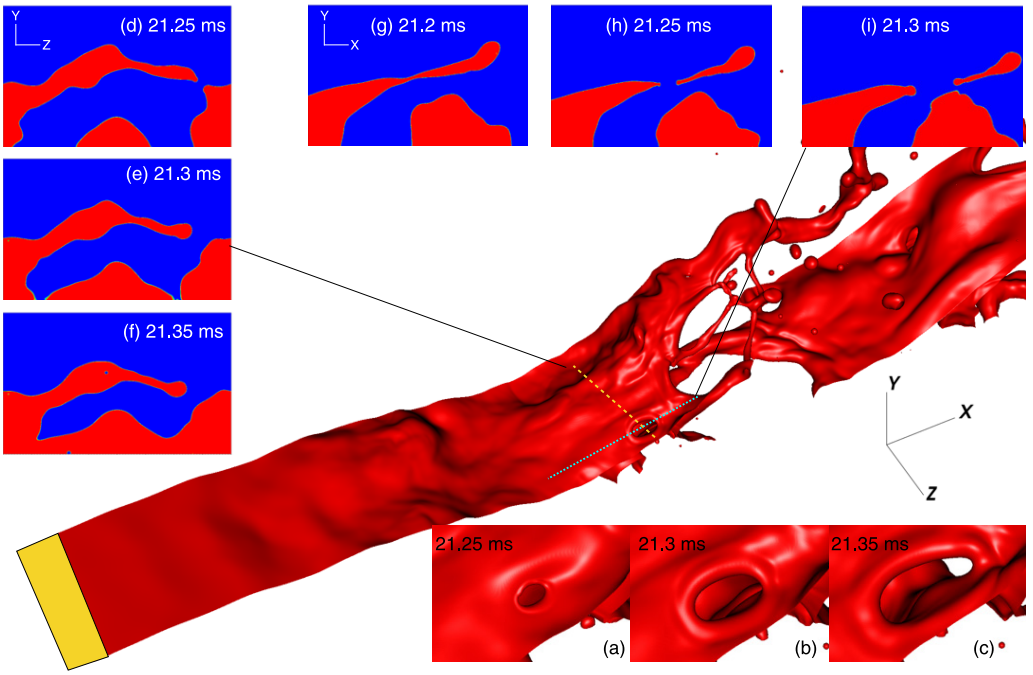

FIG. 10. Evolution of a hole formed in a liquid sheet. (a)–(c) Close-up at the hole expansion. Also shown is the liquid volume fraction (red) at the (d)–(f) y-z and (g)–(i) y-x planes cutting through the holes.

the hole appears is about 22 μm and after the sheet rupture the thickness in the vicinity of the hole varies from 27 to 85 μm. The Taylor-Culick velocity

$$U_{h,\mathrm{TC}} = \sqrt{\frac{2\sigma}{\rho_l e}} \tag{4}$$

can be calculated based on the sheet thickness, yielding $U_{h,\mathrm{TC}} = 0.95 \sim 1.68$ m/s. It can be seen that $U_{h,z}$ agrees well with $U_{h,\mathrm{TC}}$. The excess of $U_{h,x}$ over the Taylor-Culick prediction is due to the streamwise stretching the liquid sheet, which causes the hole to expand faster in the x direction than in the z direction.

It should be mentioned that the measurement of the hole expansion speed is indeed challenging. Since several holes usually form simultaneously and then merge quickly, to measure the hole expansion speed one needs to have enough time snapshots of the interface before the holes merging. Due to the high storage requirement for such large-scale simulations, this is in general quite difficult to achieve. Therefore, although many holes are observed, there is indeed a limited number of them for which we can accurately measure the expansion speed. More efficient methods in characterizing of the statistics of holes are still to be explored in future works.

Since mechanisms of sheet rupture, such as disjoining pressure, are absent in the present study, the initial formation of the holes is mesh dependent. However, it is quite clear that the subsequent hole development and the rim around the hole are well resolved with the M3 mesh. As a consequence, a further increase of mesh resolution will only delay the pinch-off point but will not affect the ligaments formed from the expansion of the holes.

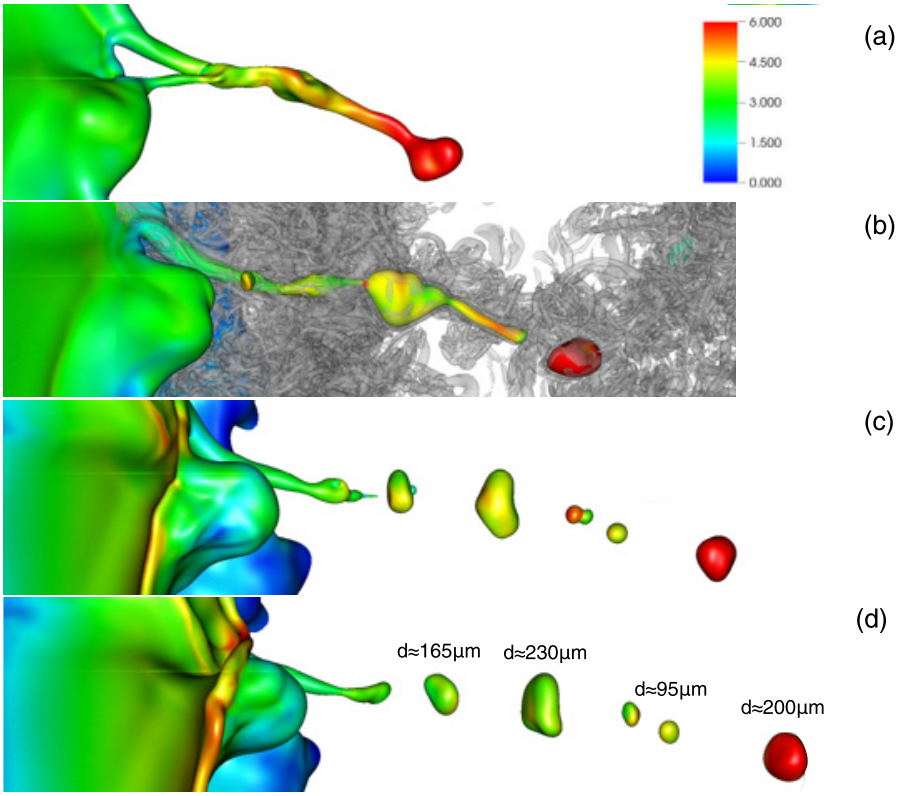

FIG. 11. Droplet generation due to ligament breakup. The turbulent vortices surrounding the ligament are plotted in (b) by the λ_2 criterion. (a) $t = 20.2$ ms, (b) $t = 20.3$ ms, (c) $t = 20.4$ ms, and (d) $t = 20.45$ ms.

E. Formation of droplets

Eventually, the ligaments break into small droplets and one realization of the breakup process is shown in Fig. 11. The ligament here is the same one as shown in Fig. 8. The ligament exhibits a very irregular shape compared to typical Rayleigh-Plateau breakup of a stationary ligament. The ligament diameter varies from 72 to 244 μm along its axis. The stretching by the surrounding turbulent gas stream [see Fig. 11(b)] clearly contributes to the irregular breakup. The neck behind the tail of the ligament pinches off, forming a big droplet of $d \approx 200\,\mu$m. The retraction of the ligament tail from the pinch-off point forms a big liquid blob in the middle of the ligament. Similar behavior is also observed in experiments [3]. Coalescence of small droplets can be seen also in Fig. 11(c). At the end, a series of droplets varying from 95 to 230 μm is produced.

To have a more general analysis of the droplets formed in atomization, we investigate the size distribution of droplets in a cubic box located downstream of the breaking wave. The sampling region is indicated in Fig. 1. The edge length of the cubic box is $2H$ ($8 \leqslant x/H \leqslant 10$, $0.5 \leqslant y/H \leqslant 2.5$, and spanning the whole width of the domain). The average number of droplets $n_d(d)$ as a function of the droplet volume-based diameter d is plotted in Figs. 12(a)–12(d), where $n_d(d)$ is defined as

$$n_d(d) = \frac{N(d)}{N_s}, \tag{5}$$

where $N(d)$ is the total number of droplets collected within the bin centered at d and N_s is the number of samples. The bin width is varied in d, starting from 6.25 μm and then increasing by a constant ratio 1.2. The reason for using wider bins for larger d is to reduce the fluctuations due to

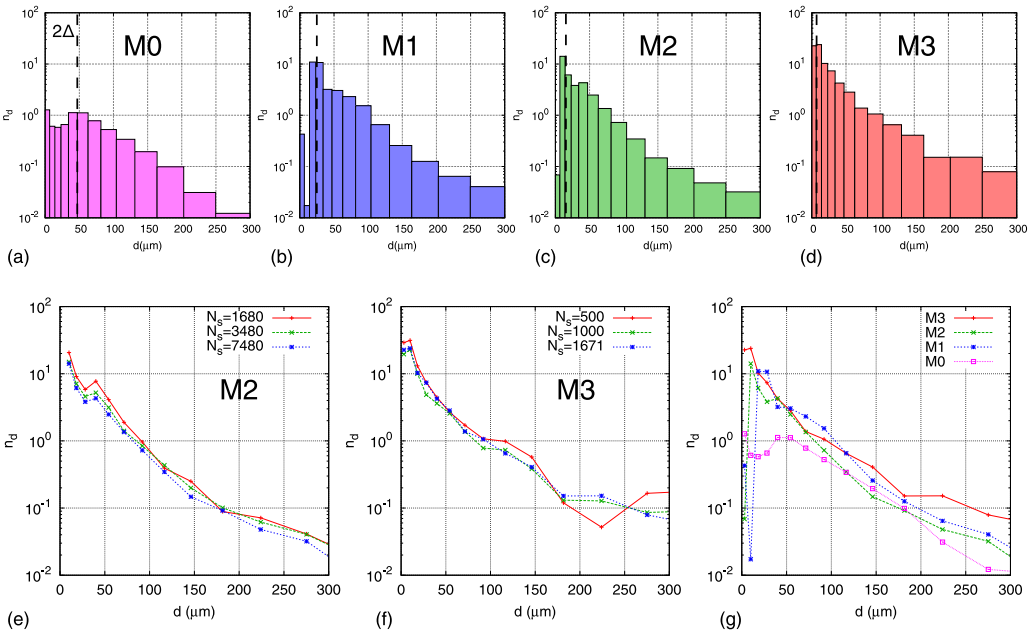

FIG. 12. Size distribution of droplet number. (a)–(d) Histograms of n_d for different meshes. The bin width increases with d by a constant ratio 1.2 from 6.25 μm. The size distribution of n_d for different sample number is shown for the (e) M2 and (f) M3 meshes, directly. Also shown is (g) the comparison of n_d for different meshes. The vertical dash lines in (a)–(d) indicate $d = 2\Delta$ for different meshes.

low numbers of larger droplets. Furthermore, it should be noted that the generation of droplets of size smaller than 2Δ for each mesh is quite likely not well captured in the present simulation. As a result, the droplets on the left of the dashed line ($d = 2\Delta$) are less trustworthy.

The droplets statistics are collected after the atomization has reached a statistically steady state (see Fig. 2) and over time intervals of about 54 ms for the M0 to M2 meshes and 5.6 ms for the M3 mesh. Sampling is conducted every 10 time steps for the M0 and M1 meshes and every 25 and 50 time steps for the M2 and M3 meshes, respectively. The sensitivity of droplet size distributions for the sample number N_s is tested for the M2 and M3 meshes [see Figs. 12(e) and 12(f)]. The size distribution of droplet number for the M2 mesh clearly converges for $N_s > 1680$ (for a sampling time interval of about 6 ms). Due to shorter simulation time for the M3 mesh, the sample number is also smaller compared to other cases. When N_s is small, such as $N_s = 500$ in Fig. 12(f), the overall trend of n_d remains similar but exhibits more fluctuations. The fluctuations are more profound for large d as the value of n_d is low. The maximum samples we collect for the M3 mesh is about $N_s = 1671$ over a time interval about 5.6 ms, during which about three to four waves break and produce droplets. From the M2 results [Fig. 12(e)] it seems like 5.6 ms is about the minimum sampling time that is required to achieve a statistically converged size distribution.

As shown in Fig. 12(g), the profiles of n_d for the M1, M2, and M3 meshes are quite similar. The M0 result is significantly different from the others, indicating that the coarse M0 mesh is insufficient for accurate prediction of droplet statistics. When the mesh size decreases, not only are more small droplets ($d \lesssim 50\,\mu$m) captured (as expected), but we also observe that more large droplets ($d \gtrsim 180\,\mu$m) are collected. These large droplets ($d \gtrsim 180\,\mu$m), such as those shown in Fig. 11, are typically generated from thicker ligaments, which are in turn produced by fingering at the end rim of the sheet (see Fig. 8) or hole-induced sheet rupture (see Fig. 9). If the mesh is not sufficiently fine to capture the Taylor-Culick rim at the edge of a liquid sheet (or at the edge of a hole) as shown in Fig. 7, then such a thick ligament may not get a chance to form. Instead, many

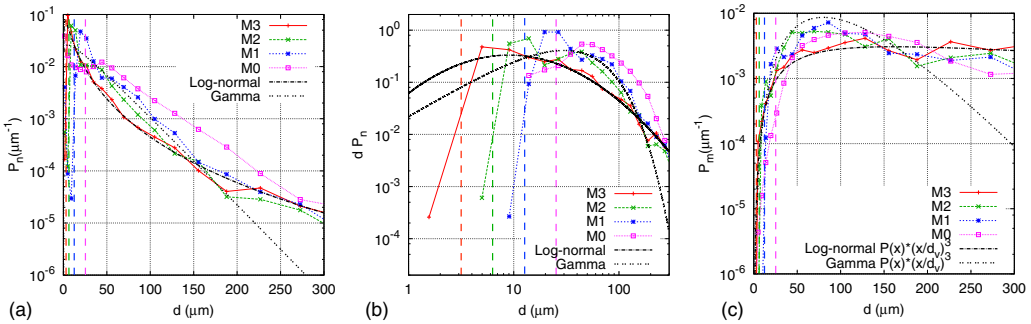

FIG. 13. Comparison of droplet (a) and (b) number and (c) mass PDF profiles with the log-normal and Γ distribution functions. The bin width increases with d by a constant ratio of 1.2 from 3.125 μm. The mesh sizes for different cases are indicted by vertical dashed lines with corresponding colors.

tiny ligaments will be produced due to numerical breakup. As a consequence, the number of large droplets appearing in the M0 result is significantly lower than that for M3.

The probability distribution function (PDF) of droplet number P_n and mass P_m is shown in Figs. 13(a) and 13(c), respectively, where P_n and P_m are defined as

$$P_n(d) = \frac{N(d)}{\Delta_d \sum N(d)} \tag{6}$$

and

$$P_m(d) = \frac{m(d)}{\Delta_d \sum m(d)}, \tag{7}$$

where Δ_d is the bin width and $m(d)$ represents the total mass of droplets collected in the bin centered at d. It can be shown that P_m can be related to P_n as

$$P_m(d) = P_n(d)\left(\frac{d}{\overline{d}_v}\right)^3, \tag{8}$$

where $\overline{d}_v$ is the mean volume-based diameter, expressed as

$$\overline{d}_v^3 = \frac{\int_0^\infty P_n(d) d^3 dd}{\int_0^\infty P_n(d) dd}. \tag{9}$$

Due to the fact that more large droplets ($d \gtrsim 180\,\mu$m) are captured when the mesh is refined, P_n is observed to be increasingly convex from M0 to M3. The shape of P_n for the M1–M3 meshes indeed agrees quite well for $d > 200\,\mu$m. It is clear that the number of tiny droplets ($d \lesssim 10\,\mu$m) increases when the mesh is refined and thus is still mesh dependent. The peak of P_n is still not well captured even with the finest mesh used here. However, these tiny droplets consist of only a small fraction of the total mass, as shown in Fig. 13(c). Compared to the droplet number distribution, for some applications the droplet mass distribution is indeed more important in characterizing sprays. It is observed that the main contribution to the mass is from droplets of $d \gtrsim 40\,\mu$m (the peak of P_m is located in $50 \lesssim d \lesssim 100\,\mu$m), which are well captured by fine meshes like M2 and M3 used in the present study.

Finally, the log-normal and Γ distribution functions are employed to fit the PDF results. The log-normal distribution function is given as

$$P_{n,L}(d) = \frac{1}{d\hat{\sigma}\sqrt{2\pi}} \exp\left[-\frac{(\ln d - \hat{\mu})^2}{2\hat{\sigma}^2}\right], \tag{10}$$

where the mean and the variance of $\ln d$ are $\hat{\mu}$ and $\hat{\sigma}^2$, respectively. The Gamma distribution can be expressed as

$$P_{n,G}(d) = \frac{\beta^\alpha}{\Gamma(\alpha)} d^{\alpha-1} \exp(-\beta d), \tag{11}$$

where $\alpha = (\tilde{\mu}/\tilde{\sigma})^2$ and $\beta = \alpha/\tilde{\mu}$, and the mean and variance of d are denoted by $\tilde{\mu}$ and $\tilde{\sigma}^2$, respectively.

A comparison between the present simulation results and the PDF models is shown in Fig. 13. The log-normal distribution is fit with $\hat{\sigma} \simeq 1.2$ and $\hat{\mu} \simeq 2.2$, while the Γ distribution is fit with $\alpha \simeq 1.2$ and $\beta \simeq 0.04$. The corresponding distributions of droplet mass for log-normal and Γ models are obtained by Eq. (8) ($\overline{d}_{v,L} = 54\,\mu$m and $\overline{d}_{v,G} = 51\,\mu$m).

Both the log-normal and Γ distributions have been observed in liquid atomization processes [6,31]. For the present simulation results, impressive agreement between the log-normal distribution and the M3 result is observed. In Fig. 13(b) we plot dP_n as a function of d on a log-log scale to show more clearly the distribution for small d. From Eq. (10) it is known that for a log-normal distribution, $\ln(dP_{n,L})$ is a parabolic function of $\ln(d)$ and the M3 results well match the right branch of the parabola. The Γ distribution fits well for $d \lesssim 150\,\mu$m for the M1 and M2 meshes, yet seems to underpredict the droplet number for large droplets.

The recent experiments by Marty [32] with a similar setup also show that the log-normal distribution is a good approximation of droplet number distribution for a wide range of parameters. The experimentally observed log-normal shape of the droplet number PDF is qualitatively consistent with the present simulation results. As shown in Eq. (10), the variance of $\ln d$, $\hat{\sigma}$, is an interesting dimensionless number to characterize the distribution profile and is independent of the mean diameter. It is also shown by Marty [32] that $\hat{\sigma}$ remains between 1 and 1.8 for a wide range of parameter combinations (M varying from about 1.5 to 16 and Re_δ from about 500 to 2000). The value of $\hat{\sigma} = 1.2$ obtained in the present simulation ($M = 20$ and $\mathrm{Re}_\delta = 2000$) lies in the range of experimentally measured values.

To further comment on these results, it is worth noting that the PDF of droplet size is indicative of the distribution of scales in two-phase turbulence. It supplements the power spectrum $P(k)$ as a rich diagnostic of the presence of large and small scales simultaneously. In the power spectrum of single-phase turbulence, an algebraic range, close to the theoretical prediction of the $k^{-5/3}$ Kolmogorov spectrum, has been observed experimentally and numerically. The ratio between the largest and the smallest wave number in that range, l_I/l_K, is a measure of the width of the spectrum and also the degree of "full" development of turbulence, where l_I and l_K are the scale of energy injection and the Kolmogorov scale, respectively. In the PDF of droplet size, a scaling with the obvious character of the Kolmogorov scaling has not been found yet. However, as some evidence points to a log-normal PDF at high velocity, the standard deviation $\hat{\sigma}$ that scales as $|\ln(d_{\min}/d_{\max})|$ then can provide a diagnostic of the presence of a wide range of scales. A large $\hat{\sigma}$ corresponds to a fully developed multiphase turbulence. The fact that $\hat{\sigma}$ falls in a similar range is an indication that the experiments and the simulations are in the same degree of full development of atomization.

In spite of the reasonable performance of the distribution models, the physical reasons for the agreement are still not fully understood. The idea behind the log-normal model is that the formation of droplets is a sequential cascade of breakups, where the larger mother drops break into smaller daughter drops. The ratio between the daughter and mother drops in each breakup is a random fractional number that follows a normal distribution. As a result, the size of the droplets formed at the end follows a log-normal distribution. In contrast to the breakup process, the coalescence between droplets introduces an inverse cascade, i.e., smaller droplets collide and merge to form bigger droplets or the coalescence of the smaller blobs constitutive of a ligament form bigger blobs. These aggregation scenarios will result in a Γ distribution for the droplet size [6]. The simulations presented here show that the spray formation is through a sequence of different complex mechanisms and neither of these two PDF models is therefore likely to completely capture these mechanisms.

We have observed breakups in sequence: The bulk liquid first breaks into thin liquid sheets, then the sheets into fingers and ligaments, and at last the ligaments into droplets of different size. However, the process of spray formation is clearly not a sequence of random breakups like suggested in the log-normal distribution model. (We rarely see a droplet, once formed, further break into smaller droplets in the fine mesh runs.) On the other hand, coalescence of droplets, the assumption behind the Γ distribution model, is only occasionally observed. Therefore, it is also quite likely that the aggregation would not have a significant impact on the droplet size either.

Notice that both of these classical distributions, the log-normal and the Γ, are obtained when a scaling process is observed, that is, when nonlinear effects occur over a large range of scales. For example, Kolmogorov turbulent cascade for the log-normal distribution and Einstein-Smoluchowski aggregation dynamics for the Γ distribution, both span a wide range of scales from $\ell_{\min}$ to $\ell_{\max}$. The fact that $\ln(\ell_{\max}/\ell_{\min})$ is large is a condition of applicability of the central limit theorem in these theories. Here the best fit to the log-normal distribution indicates that $\ln(\ell_{\max}/\ell_{\min}) \sim 2\hat{\sigma} \approx 2.4$. Compared to many scaling observations performed in physics over a moderate range of scales, to be specific with just one decade as $\ln(\ell_{\max}/\ell_{\min}) \geqslant \ln 10 \approx 2.3$, the present system has a sufficiently large range of scales to consider scaling hypotheses, but not yet a "truly" large range of scales as in Kolmogorov turbulent cascade experiments at large Reynolds numbers. The absence of a truly large range of scales makes it difficult to draw definite conclusions from the fit of the droplet size probability distribution to the classical theories, but it also indicates that none of these theories is without doubt in its range of validity.

Another analysis of the droplet size distributions that does not involve a single scaling process is to consider several distinct processes at different scales, for instance, rim drops from the disintegration of the Taylor-Culick rims and film drops from the disintegration of the thin sheets. In some experiments [4] hints of the bimodal distributions that would result from two distinct processes have been seen. We observe no such effects in our distributions.

IV. CONCLUSION

Spray formation in a gas-liquid mixing layer was investigated by DNS in the present study. To examine whether the simulation fully resolves all the physical scales, the mesh resolution was varied and the finest mesh consisted of about 4×10^9 cells. The simulation results clearly show the detailed processes of how the bulk liquid jet breaks into sheets, then ligaments, and finally droplets. The development of the interfacial wave is crucial to the sheet formation. Both quasi-2D and fully 3D waves were observed. For the 3D waves, the development of the 3D structure was clearly much faster than the Rayleigh-Plateau instability in the end rim. Ligaments were shown to be generated by fingering at end rims of liquid sheets and also by expansion of holes in liquid sheets. A sequence of hole evolutions were shown and the measured expansion velocity was found to agree well with the Taylor-Culick theory. Due to the interaction with the surrounding turbulent gas stream, ligaments generally exhibit irregular shapes and complex dynamics when they break into droplets. The size distributions of droplets in a sampling box downstream of the breaking wave were investigated for different meshes. It was found that the coarse M0 mesh will miss not only the small droplets, but also the larger ones. The reason is that if the development of the wave is not well resolved (the mesh is not sufficiently fine for the curvature of the wave crest or the shear layer above the wave), the sheet formation will be erroneous, resulting in fake breakups and many tiny ligaments and drops, instead of larger droplets and thicker ligaments as observed in the fine mesh results. Finally, the log-normal and Γ distributions were employed to fit the PDF data and the log-normal model seems to fit better with the simulation results of the fine meshes.

ACKNOWLEDGMENTS

This project was supported by the ANR MODEMI project (No. ANR-11-MONU-0011) program and the FIRST project supported by the European Commission under the 7th Framework Programme

under Grant Agreement No. 265848. This work was granted access to the HPC resources of TGCC-CURIE under the allocations x20152b7325 and t20162b7760 made by GENCI. We would also acknowledge PRACE (2014112610) for awarding us access to CINECA-FERMI and to LRZ-SuperMUC based in Italy and Germany.

---

[1] J. C. Lasheras and E. J. Hopfinger, Liquid jet instability and atomization in a coaxial gas stream, Annu. Rev. Fluid Mech. **32**, 275 (2000).
[2] J. Eggers and E. Villermaux, Physics of liquid jets, Rep. Prog. Phys. **71**, 036601 (2008).
[3] E. Villermaux, P. Marmottant, and J. Duplat, Ligament-Mediated Spray Formation, Phys. Rev. Lett. **92**, 074501 (2004).
[4] P. Marmottant and E. Villermaux, On spray formation, J. Fluid Mech. **498**, 73 (2004).
[5] J. Hoepffner, R. Blumenthal, and S. Zaleski, Self-Similar Wave Produced by Local Perturbation of the Kelvin-Helmholtz Shear-Layer Instability, Phys. Rev. Lett. **106**, 104502 (2011).
[6] E. Villermaux, Fragmentation, Annu. Rev. Fluid Mech. **39**, 419 (2007).
[7] L. Opfer, I. V. Roisman, J. Venzmer, M. Klostermann, and C. Tropea, Droplet-air collision dynamics: Evolution of the film thickness, Phys. Rev. E **89**, 013023 (2014).
[8] J. O. Marston, T. T. Truscott, N. B. Speirs, M. M. Mansoor, and S. T. Thoroddsen, Crown sealing and buckling instability during water entry of spheres, J. Fluid Mech. **794**, 506 (2016).
[9] J.-P. Matas, S. Marty, and A. Cartellier, Experimental and analytical study of the shear instability of a gas-liquid mixing layer, Phys. Fluids **23**, 094112 (2011).
[10] J. J. S. Jerome, S. Marty, J.-P. Matas, S. Zaleski, and J. Hoepffner, Vortices catapult droplets in atomization, Phys. Fluids **25**, 112109 (2013).
[11] J.-P. Matas, S. Marty, M. S. Dem, and A. Cartellier, Influence of Gas Turbulence on the Instability of an Air-Water Mixing Layer, Phys. Rev. Lett. **115**, 074501 (2015).
[12] D. Fuster, J.-P. Matas, S. Marty, S. Popinet, J. Hoepffner, A. Cartellier, and S. Zaleski, Instability regimes in the primary breakup region of planar coflowing sheets, J. Fluid Mech. **736**, 150 (2013).
[13] M. Gorokhovski and M. Herrmann, Modeling primary atomization, Annu. Rev. Fluid Mech. **40**, 343 (2008).
[14] R. Lebas, T. Menard, P. A. Beau, A. Berlemont, and F.-X. Demoulin, Numerical simulation of primary break-up and atomization: DNS and modeling study, Int. J. Multiphase Flow **35**, 247 (2009).
[15] J. Shinjo and A. Umemura, Simulation of liquid jet primary breakup: Dynamics of ligament and droplet formation, Int. J. Multiphase Flow **36**, 513 (2010).
[16] G. Tryggvason, R. Scardovelli, and S. Zaleski, *Direct Numerical Simulations of Gas-Liquid Multiphase Flows* (Cambridge University Press, Cambridge, 2011).
[17] E. Aulisa, S. Manservisi, R. Scardovelli, and S. Zaleski, Interface reconstruction with least-squares fit and split advection in three-dimensional Cartesian geometry, J. Comput. Phys. **225**, 2301 (2007).
[18] J. Li, Calcul d'interface affine par morceaux (piecewise linear interface calculation), C. R. Acad. Sci. Paris Ser. IIB **320**, 391 (1995).
[19] R. Scardovelli and S. Zaleski, Interface reconstruction with least-square fit and split Eulerian-Lagrangian advection, Int. J. Numer. Meth. Fluids **41**, 251 (2003).
[20] M. Rudman, A volume-tracking method for incompressible multifluid flows with large density variations, Int. J. Numer. Methods Fluids **28**, 357 (1998).
[21] S. Popinet, An accurate adaptive solver for surface-tension-driven interfacial flows, J. Comput. Phys. **228**, 5838 (2009).
[22] Y. Renardy and M. Renardy, PROST: A parabolic reconstruction of surface tension for the volume-of-fluid method, J. Comput. Phys. **183**, 400 (2002).
[23] M. M. Francois, S. J. Cummins, E. D. Dendy, D. B. Kothe, J. M. Sicilian, and M. W. Williams, A balanced-force algorithm for continuous and sharp interfacial surface tension models within a volume tracking framework, J. Comput. Phys. **213**, 141 (2006).

[24] Y. Ling, S. Zaleski, and R. Scardovelli, Multiscale simulation of atomization with small droplets represented by a Lagrangian point-particle model, Int. J. Multiphase Flow **76**, 122 (2015).
[25] T. J. Arrufat, S. Dabiri, D. Fuster, Y. Ling, L. Malan, R. Scardovelli, G. Tryggvason, P. Yecko, and S. Zaleski, PARIS code, available at http://www.ida.upmc.fr/~zaleski/paris
[26] I. V. Roisman, K. Horvat, and C. Tropea, Spray impact: Rim transverse instability initiating fingering and splash, and description of a secondary spray, Phys. Fluids **18**, 102104 (2006).
[27] G. Agbaglah, C. Josserand, and S. Zaleski, Longitudinal instability of a liquid rim, Phys. Fluids **25**, 022103 (2013).
[28] P. Yecko and S. Zaleski, Transient growth in two-phase mixing layers, J. Fluid Mech. **528**, 43 (2005).
[29] X. Wu and P. Moin, Direct numerical simulation of turbulence in a nominally zero-pressure-gradient flat-plate boundary layer, J. Fluid Mech. **630**, 5 (2009).
[30] S. K. Robinson, Coherent motions in the turbulent boundary layer, Annu. Rev. Fluid Mech. **23**, 601 (1991).
[31] O. Sotolongo-Costa, Y. Moreno-Vega, J. J. Lloveras-González, and J. C. Antoranz, Criticality in Droplet Fragmentation, Phys. Rev. Lett. **76**, 42 (1996).
[32] S. Marty, Contribution a l'étude de l'atomisation assistée d'un liquide, Ph.D. thesis, Université de Grenoble, 2015.